LETTERS

Slow dust in Enceladus' plume from condensation and wall collisions in tiger stripe fractures

Jürgen Schmidt[1], Nikolai Brilliantov[1,2,3], Frank Spahn[1] & Sascha Kempf[4,5]

One of the spectacular discoveries of the Cassini spacecraft was the plume of water vapour and icy particles (dust) originating near the south pole of Saturn's moon Enceladus[1–5]. The data imply considerably smaller velocities for the grains[2,5,6] than for the vapour[4,7], which has been difficult to understand. The gas and dust are too dilute in the plume to interact, so the difference must arise below the surface. Here we report a model for grain condensation and growth in channels of variable width. We show that repeated wall collisions of grains, with re-acceleration by the gas, induce an effective friction, offering a natural explanation for the reduced grain velocity. We derive particle speed and size distributions that reproduce the observed and inferred properties of the dust plume. The gas seems to form near the triple point of water; gas densities corresponding to sublimation from ice at temperatures less than 260 K are generally too low to support the measured particle fluxes[2]. This in turn suggests liquid water below Enceladus' south pole.

The structure of Saturn's E ring clearly points at Enceladus as its main source[8,9] and the early prediction of cryo-volcanic activity[10–12] was recently confirmed by Cassini data[1–5]. Enceladus' plume originates from sources in the south polar region, located on four linear structures[5,13–15] (dubbed 'tiger stripes'), which probably form the outlets of a system of cracks in the moon's ice shell through which water vapour escapes to vacuum from subsurface sites of evaporation. Although the gas expands to space[4,7] with a speed of 300–500 m s^{-1}, most grains are ejected at speeds[2,5,6] smaller than

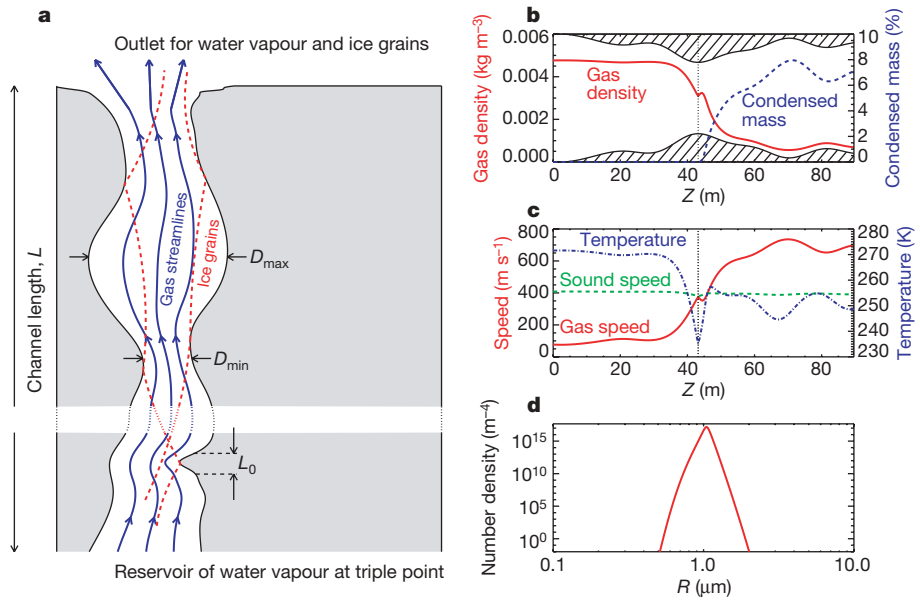

Figure 1 | Gas flow and condensation in cracks in Enceladus' ice shell. **a**, Schematic sketch. Gas escapes through channels of variable cross-section to vacuum from a reservoir at the triple point of water. Channel profiles are constructed as superposition of random harmonics (Supplementary equations S11–S14), with smallest length scale L_0, for a given total length L, and minimal and maximal channel widths D_{min} and D_{max}. Because the equations describing the channel flow and condensation are invariant under the transformation $D \to \alpha D$, for any positive factor α, we may choose D_{max} arbitrarily for fixed D_{min}/D_{max}. Eventually, we identify D_{max} with the collision length L_{coll}, which must be of the same order. From the condensation model the particle speed–size distribution is obtained as an average over an ensemble of 5,000 individual channel solutions. **b**, Typical solution for gas density and mass fraction of condensed grains along a channel of length 90 m, $D_{min}/D_{max} = 0.56$, and $L_0 = 18.76$ m. The position in the channel is denoted by Z. The density drops drastically near the narrowest point of the channel (nozzle throat), where most grains nucleate. **c**, Profiles of gas speed and temperature. The transition to supersonic flow occurs near the nozzle throat, displaced slightly downstream owing to condensation. Cooling in the nozzle zone leads to a drastic increase of supersaturation and condensation. Owing to the latent heat, the temperature rises again. **d**, Particle number density per radius increment for one single channel. Other random channels (varying L_0 and D_{min}/D_{max}) yield distributions with peak sizes between tens of nanometres and tens of micrometres (Supplementary Fig. 3).

[1]Nichtlineare Dynamik, Universität Potsdam, Am Neuen Palais 10, 14469 Potsdam, Germany. [2]Department of Mathematics, University of Leicester, Leicester LE1 7RH, UK. [3]Department of Physics, Moscow State University, 119991 Moscow, Russia. [4]Max Planck Institut für Kernphysik, 69117 Heidelberg, Germany. [5]IGEP, Technische Universität Braunschweig, 38106 Braunschweig, Germany.

Enceladus' escape velocity of 240 m s^{-1}. Such a difference would appear plausible for a non-stationary (for example, explosive) process but it is not expected for the observed quasi-stationary particle[15] and gas fluxes. Moreover, neither this dynamical difference nor the dust formation may be attributed to processes outside the satellite: here the gas is extremely dilute and practically collision-free[4,7]. Hence the grains must form inside the satellite.

Existing models suggest that simultaneous freezing and boiling of near-surface water[5,6], suddenly exposed to vacuum, leads to ejection of vapour and grains. However, in this framework the stationarity of the plumes is difficult to understand. Models based on decomposition of clathrates[16,17] can explain the observed abundances of volatile gases[3] but the formation of dust grains (speed and size distribution) is not quantified. Here we show that grain condensation in the subsurface gas flow is consistent with the observed properties of the dust plume[2,5], and the inferred gas speeds and production rates[3,4,7]. Just as in a nozzle, the variation of the channel width causes transition to supersonic speeds and locally enhanced condensation (Fig. 1). Moreover, in a non-straight channel the streamlines of dilute vapour and grains generally differ (Fig. 1a). Thus, directional changes of the gas flow (imposed by the cracks) and wall collisions will lead to an effective deceleration of grains relative to the gas.

We model this effect as a Poisson random process with flight times t exponentially distributed as $\exp[-t/(L_{\mathrm{coll}}/u_{\mathrm{gas}})]$, where L_{coll} defines the characteristic length between collisions and u_{gas} is the gas speed. Grains are re-accelerated with a rate depending on gas density and particle radius R (Fig. 2). We obtain (Supplementary Information) their velocity distribution $P(u_{\mathrm{grain}})$:

$$P(u_{\mathrm{grain}}) = \frac{R}{R_{\mathrm{c}}}\left[1+\frac{R}{R_{\mathrm{c}}}\right]\frac{u_{\mathrm{grain}}}{u_{\mathrm{gas}}}\left[1-\frac{u_{\mathrm{grain}}}{u_{\mathrm{gas}}}\right]^{\frac{R}{R_{\mathrm{c}}}-1} \quad (1)$$

and their average speed as a function of radius R:

$$\langle u_{\mathrm{grain}}(R)\rangle = \left(1+\frac{R}{2R_{\mathrm{c}}}\right)^{-1} u_{\mathrm{gas}} \quad (2)$$

where we define the critical radius R_{c}:

$$R_{\mathrm{c}} \equiv \frac{\rho_{\mathrm{gas}}}{\rho_{\mathrm{grain}}}\sqrt{\frac{8k_B T_{\mathrm{gas}}}{\pi m_0}}\left[1+\frac{\pi}{8}(1-\beta)\right]\frac{L_{\mathrm{coll}}}{u_{\mathrm{gas}}} \quad (3)$$

separating slow and fast particles (see Fig. 2 for notation). The condensation coefficient β, ranging[18,19] from 0.1 to 1, quantifies the adsorption of water molecules by growing grains, so that their growth rate is proportional to β. For gas near the triple point of water and L_{coll} of the order of decimetres we find R_{c} in the submicrometre range. In this case submicrometre-sized dust particles escape the vent essentially at the gas speed, while larger grains are slower, with $\langle u_{\mathrm{grain}}(R)\rangle \propto 1/R$.

The expanding vapour is super-saturated and by condensation its density will adjust rapidly close to the saturated value $\rho_{\mathrm{eq}}(T_{\mathrm{gas}})$ at temperature T_{gas} (Fig. 2). Using equations (2) and (3) we obtain a relation between the collision length L_{coll} and temperature, which shows that $\langle u_{\mathrm{grain}}\rangle$ increases with L_{coll}. Basically, $\langle u_{\mathrm{grain}}\rangle$ is determined by the brightness gradient of the plume[6]. To fix ideas, we take $\langle u_{\mathrm{grain}}\rangle = 100$ m s^{-1} for micrometre-sized grains, which, as shown below, is consistent with plume brightness and observed particle number density (Fig. 3). In this way we obtain a lower bound for possible L_{coll} (Fig. 2). If the collision length, roughly determined by the width of the cracks, is smaller than this bound, the gas is too dilute to support the observed particle flux. For gas temperatures below ~170 K the mean free path must exceed 10 km, which requires implausibly wide or straight cracks. More plausible channel widths between decimetres and metres, implying collision lengths of the same order, require temperatures between 240 and 260 K (Fig. 2). The expanding gas cools by a few tens of degrees (Supplementary Fig. 3), so that the actual temperatures at the site of evaporation must be 260 K or higher. Hence, a crack width of decimetres (Fig. 3) implies the presence of liquid water. We note that this conclusion is independent of the process of grain formation.

The large surface temperatures near the 'tiger stripes'[13,14] and evidence for hot chemistry[20] provide additional support for the presence of liquid water in equilibrium with ice and vapour (the triple point) below the south polar terrain[5,21,22]. Hence, we combine hydrodynamic equations and the first thermodynamic law to model condensation in water vapour (Supplementary Information) that expands from triple point conditions through channels of variable width (Fig. 1a). As the expanding gas cools, it becomes supersaturated, and efficient condensation into the solid phase sets in, typically limited to a narrow region (Supplementary Fig. 2). For the precise description of the homogeneous nucleation rate we employ a fit to experimental data for water[23] (Fig. 2). We obtain a closed set of equations (Supplementary equations S1–S4, S6, S7 and S10) for density, temperature and speed of the gas, as well as for the mass fraction and size of condensed grains along the channel (Fig. 1).

To account for natural geometric variety, we generate a large number (5,000) of random channels (Fig. 1). We combine the size distribution from individual channel profiles with the speed distribution (equation (1)) and average it over the ensemble of random channels. The resulting speed–size distribution is independent of the total channel length, provided the length is much larger than the maximal width of the cracks (Supplementary Fig. 7). From this distribution we generate starting conditions for three-body integrations and construct a computer model of the plume. Starting positions and directions are, respectively, uniformly distributed in a circular area of 10° half-angle around Enceladus' south pole and in a cone of 25° half-angle about the surface normal. Trajectories are followed numerically until the particles reach a distance of two Hill radii (sphere of gravitational influence, $r_{\mathrm{H}} = 948$ km) or they strike the moon again. The total flux of grains is normalized such that the model reproduces the peak number density 0.08 m^{-3} of particles with $R > 1.6$ μm recorded by the Cassini High Rate Detector (HRD) on the trajectory of the

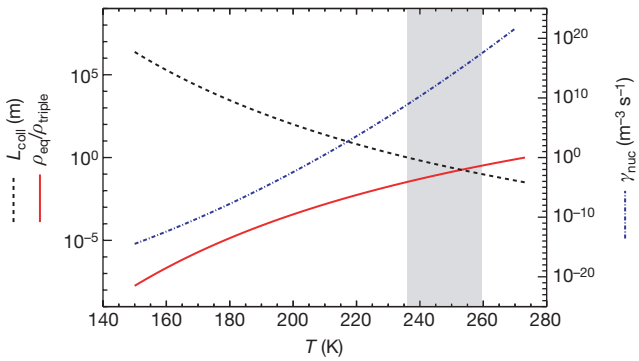

Figure 2 | Temperature dependence of grain dynamics and homogeneous nucleation rate. Ice grains move between random wall collisions according to the equation: $\dot{u}_{\mathrm{grain}} = \left(1+\frac{\pi}{8}[1-\beta]\right)\frac{\rho_{\mathrm{gas}}}{\rho_{\mathrm{grain}}}\sqrt{\frac{8k_B T_{\mathrm{gas}}}{\pi m_0}}\left(u_{\mathrm{gas}}-u_{\mathrm{grain}}\right)$. For exponentially distributed flight times this yields the distribution (equation (1)) (Supplementary equations S17–S19). Here $\rho_{\mathrm{grain}} = 920$ kg m^{-3} and u_{grain} are the material density and the speed of the grains, ρ_{gas}, u_{gas} and T_{gas} are the density, the speed and the temperature of the gas, k_{B} is Boltzmann's constant, and m_0 is the mass of a water molecule. The dashed curve gives a lower bound for L_{coll} necessary to maintain a mean speed $\langle u_{\mathrm{grain}}\rangle$ for micrometre-sized particles that is larger than 100 m s^{-1}. We use $u_{\mathrm{gas}} = 500$ m s^{-1} and $\rho_{\mathrm{gas}} = \rho_{\mathrm{eq}}(T_{\mathrm{gas}})$ (shown as solid red curve, $\rho_{\mathrm{triple}} = 4.85$ g m^{-3}), the saturated vapour density for given temperature. The temperature range for which 0.1 m $< L_{\mathrm{coll}} <$ 1 m is shaded in grey. For the homogeneous nucleation rate we use the relation $\gamma_{\mathrm{nuc}} = B(T_{\mathrm{gas}})(\sigma-1)^{n(T_{\mathrm{gas}})}$ with the supersaturation $\sigma = \rho_{\mathrm{gas}}/\rho_{\mathrm{eq}}(T_{\mathrm{gas}})$. The temperature dependence of the coefficients $B(T_{\mathrm{gas}})$ and $n(T_{\mathrm{gas}})$ (Supplementary equations S8 and S9) we obtain from fits to experimental data[23]. The nucleation rate drops drastically with decreasing temperature (dash-dotted curve, shown for fixed $\sigma = 10$).

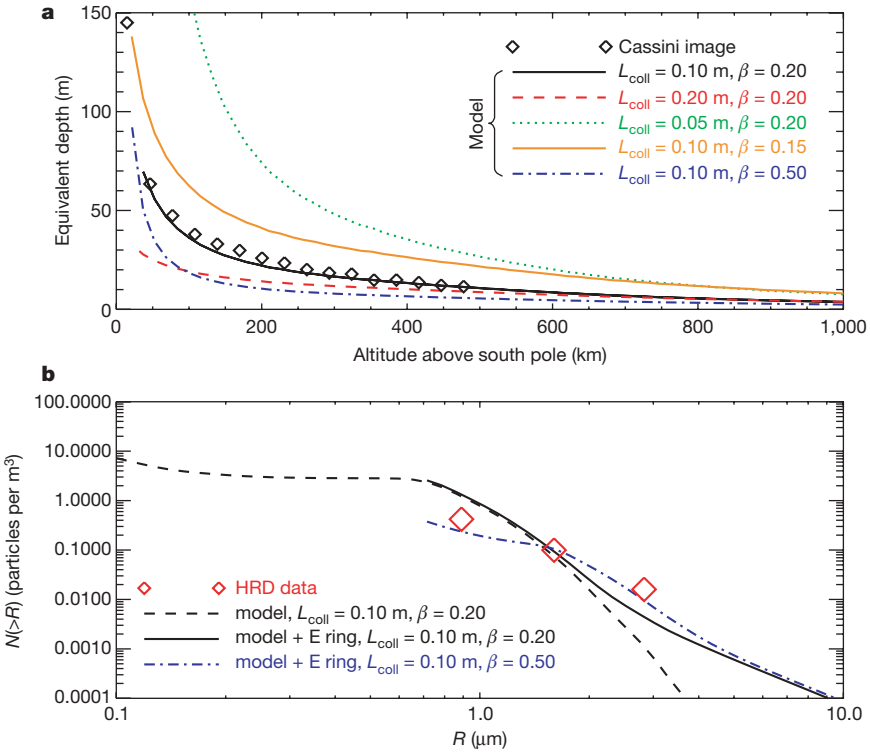

Figure 3 | Comparison of model results with Cassini data. a, Brightness of the model plume (phase angle 153°, wavelength 750 nm) with a Cassini image from February 2005 (N1487334245_1, phase angle 153°, IR1 filter λ_{eff} = 751 nm). At this time Enceladus was near its pericentre, as it was at the time of the fly-by when the HRD data was recorded. Thus, the plume's level of activity should be comparable, if it varies with the orbital phase of Enceladus[27]. Background brightness due to E ring dust has been subtracted (Supplementary Information). Equivalent depth—that is, brightness integrated along image lines, $\int (I/F)dx$, orthogonal to the plume axis—is plotted versus altitude (symbols). The profile of equivalent depth for the model plume, computed from Mie theory, is overplotted (lines). The brightness of the model depends mainly on collision length L_{coll} and condensation coefficient β (see also Supplementary Figs 5 and 7). **b**, Cumulative particle size distribution from the model (dashed line) at the location where the HRD measured the maximal particle density (Cassini fly-by E11). The solid line includes an estimate for the background due to E ring particles[2,28] in the range $R > 0.8$ μm. The number densities N of particles larger than 0.9, 1.6 and 2.8 μm, respectively, derived from the *in situ* data[2], are shown as diamond symbols.

Enceladus fly-by[2] in July 2005 (Fig. 3b). We reconstruct an image of the model plume (Supplementary Fig. 6) from Mie theory for smooth spheres (we use Mishchenko's Mie code: http://www.giss.nasa.gov/~crmim). The parameters β and L_{coll} are fixed by comparison to the brightness and the brightness gradient in Cassini images (Fig. 3a, Supplementary Fig. 6). A good agreement is obtained for $\beta = 0.2$ and $L_{coll} = 0.1$ m.

For the example shown in Fig. 3, the minimal widths and shortest scales (Fig. 1a) for the ensemble of random channels are drawn uniformly from the intervals $0.3 < D_{min}/D_{max} < 0.9$ and $5\,m < L_0 < 40\,m$ and the total length is fixed to $L = 150$ m. Variation of interval boundaries and channel length L results in mild quantitative changes (Supplementary Fig. 7) of the curves of Fig. 3. A similarly small effect results from plausible variation of the area of particle ejection around the south pole and the width of the ejection cone.

With the HRD data we adjust the total dust flux, proportional to the venting-active surface, to obtain a value for this area of 200 m^2. A channel width ($D_{max} \approx L_{coll}$) of the order of 10 cm then yields a total venting active length of 2 km along the 'tiger stripes' (total length 500 km), consistent with the observation of isolated sources[13,15]. The total dust production rate is about 5 kg s^{-1} of which ~10% escapes the satellite, in agreement with estimates of 1 kg s^{-1} for the mass loss rate of the E ring[24]. Slightly more than half of the escaping mass is in particles larger than 1 μm. The mean fraction of condensed mass $\langle f \rangle \approx 0.06$ (Supplementary Fig. 3) then gives roughly 100 kg s^{-1} of gas production, which is in reasonable agreement with the 150–300 kg s^{-1} inferred from occultation data obtained by the Cassini Ultraviolet Imaging Spectrograph[4] and the Ion and Neutral Mass Spectrometer[3]. If this amount of gas condenses at the walls[22] of kilometre-long channels, we obtain a timescale of months for self-sealing. Our theory predicts particle sizes in the micrometre range (Fig. 3b, Supplementary Figs 4 and 5) with a local peak around 0.8 μm and a steep decay towards larger sizes. The HRD data shows a shallower slope due to the background of E ring particles: Large grains have larger orbital lifetimes[24–26] than small ones, and thus, once having escaped from the moon, they become more abundant in the E ring than in the plume.

Received 5 June; accepted 15 November 2007.

1. Dougherty, M. K. *et al.* Identification of a dynamic atmosphere at Enceladus with the Cassini magnetometer. *Science* **311**, 1406–1409 (2006).
2. Spahn, F. *et al.* Cassini dust measurements at Enceladus and implications for the origin of the E ring. *Science* **311**, 1416–1418 (2006).
3. Waite, J. H. *et al.* Cassini ion and neutral mass spectrometer: Enceladus plume composition and structure. *Science* **311**, 1419–1422 (2006).
4. Hansen, C. J. *et al.* Enceladus' water vapor plume. *Science* **311**, 1422–1425 (2006).
5. Porco, C. C. *et al.* Cassini observes the active south pole of Enceladus. *Science* **311**, 1393–1401 (2006).
6. Ingersoll, A. P., Porco, C. C., Helfenstein, P., West, R. A., the Cassini ISS Team. Models of the Enceladus plumes. *Bull. Am. Astron. Soc.* **38**, 508 (2006).
7. Tian, F., Stewart, A. I. F., Toon, O. B., Larsen, K. W. & Esposito, L. W. Monte Carlo simulations of the water vapor plumes on Enceladus. *Icarus* **188**, 154–161 (2007).
8. Showalter, M., Cuzzi, J. & Larson, S. Structure and particle properties of Saturn's E ring. *Icarus* **94**, 451–473 (1991).
9. Nicholson, P. D. *et al.* Observations of Saturn's ring-plane crossing in August and November 1995. *Science* **272**, 509–516 (1996).
10. Haff, P. K., Eviatar, A. & Siscoe, G. Ring and plasma: the enigmae of Enceladus. *Icarus* **56**, 426–438 (1983).
11. Pang, K. D., Voge, C. C., Rhoads, J. W. & Ajello, J. M. The E ring of Saturn and satellite Enceladus. *J. Geophys. Res.* **89**, 9459–9470 (1984).

12. Kargel, J. S. & Pozio, S. The volcanic and tectonic history of Enceladus. *Icarus* **119,** 385–404 (1996).
13. Spencer, J. R. *et al.* Cassini encounters Enceladus: background and the discovery of a south polar hot spot. *Science* **311,** 1401–1405 (2006).
14. Brown, R. H. *et al.* Composition and physical properties of Enceladus. *Surf. Sci.* **311,** 1425–1428 (2006).
15. Spitale, J. N. & Porco, C. C. Association of the jets of Enceladus with the warmest regions on its south-polar fractures. *Nature* **449,** 695–697 (2007).
16. Kieffer, S. W. *et al.* A clathrate reservoir hypothesis for Enceladus' south polar plume. *Science* **314,** 1764–1766 (2006).
17. Gioia, G., Chakraborty, P., Marshak, S. & Kieffer, S. W. Unified model of tectonics and heat transport in a frigid Enceladus. *Proc. Natl Acad. Sci. USA* **104,** 13578–13591 (2007).
18. Shaw, R. A. & Lamb, D. Experimental determination of the thermal accommodation and condensation coefficients of water. *J. Chem. Phys.* **111,** 10659–10663 (1999).
19. Batista, E. R., Ayotte, P., Bilic, A., Kay, B. D. & Jonsson, H. What determines the sticking probability of water molecules on ice? *Phys. Rev. Lett.* **95,** 223201 (2005).
20. Matson, D. L., Castillo, J. C., Lunine, J. & Johnson, T. V. Enceladus' plume: compositional evidence for a hot interior. *Icarus* **187,** 569–573 (2007).
21. Collins, G. C. & Goodman, J. C. Enceladus' south polar sea. *Icarus* **189,** 72–82 (2007).
22. Nimmo, F., Spencer, J. R., Pappalardo, R. T. & Mullen, M. E. Shear heating as the origin of the plumes and heat flux on Enceladus. *Nature* **447,** 289–291 (2007).
23. Viisanen, Y., Strey, R. & Reiss, H. Homogeneous nucleation rates for water. *J. Chem. Phys.* **99,** 4680–4692 (1993).
24. Juhász, A. & Horányi, M. Saturn's E ring: a dynamical approach. *J. Geophys. Res.* **107,** 1–10 (2002).
25. Horányi, M., Burns, J. A. & Hamilton, D. P. The dynamics of Saturn's E ring particles. *Icarus* **97,** 248–259 (1992).
26. Hamilton, D. & Burns, J. Origin of Saturn's E ring: selfsustained—naturally. *Science* **264,** 550–553 (1994).
27. Hurford, T. A., Helfenstein, P., Hoppa, G. V., Greenberg, R. & Bills, B. G. Eruptions arising from tidally controlled periodic openings of rifts on Enceladus. *Nature* **447,** 292–294 (2007).
28. Kempf, S. *et al.* The E ring in the vicinity of Enceladus I: spatial distribution and properties of the ring particles. *Icarus*. (in the press).

Supplementary Information is linked to the online version of the paper at www.nature.com/nature.

Acknowledgements We thank M. Burton, P. Krapivsky, H. Salo, T. Spilker, M. Sremčević and F. Tian for discussions. We acknowledge the efforts of the Cassini ISS team in the design and operation of the ISS instrument. This work was supported by Deutsches Zentrum für Luft und Raumfahrt and Deutsche Forschungsgemeinschaft.

Author Information Reprints and permissions information is available at www.nature.com/reprints. Correspondence and requests for materials should be addressed to J.S. (jschmidt@agnld.uni-potsdam.de).